

Folate Receptor-Targeted, ROS-Responsive Dextran-Block-Poly (propylene sulfide) Copolymer Nanoparticles: A Bioinformatics-Guided Approach for Prostate Cancer Therapy

Yixun Zhang¹, Zhenguo Liang², Zeheng Tan³, Jundong Lin⁴, Xinqing Jiang¹, Ruimeng Yang¹, Jian Zhang¹, Huijing Tan¹, Wenjie Xie¹, Yangjia Zhuo¹, Fen Zou¹, Jianheng Ye¹, Jianming Lu¹, Yingke Liang¹, Ronghua Yang¹, Weide Zhong¹, and Hui-Kang Yang¹

¹the Second Affiliated Hospital, School of Medicine, South China University of Technology

²the First Affiliated Hospital of Guangzhou Medical University, Guangzhou Medical University

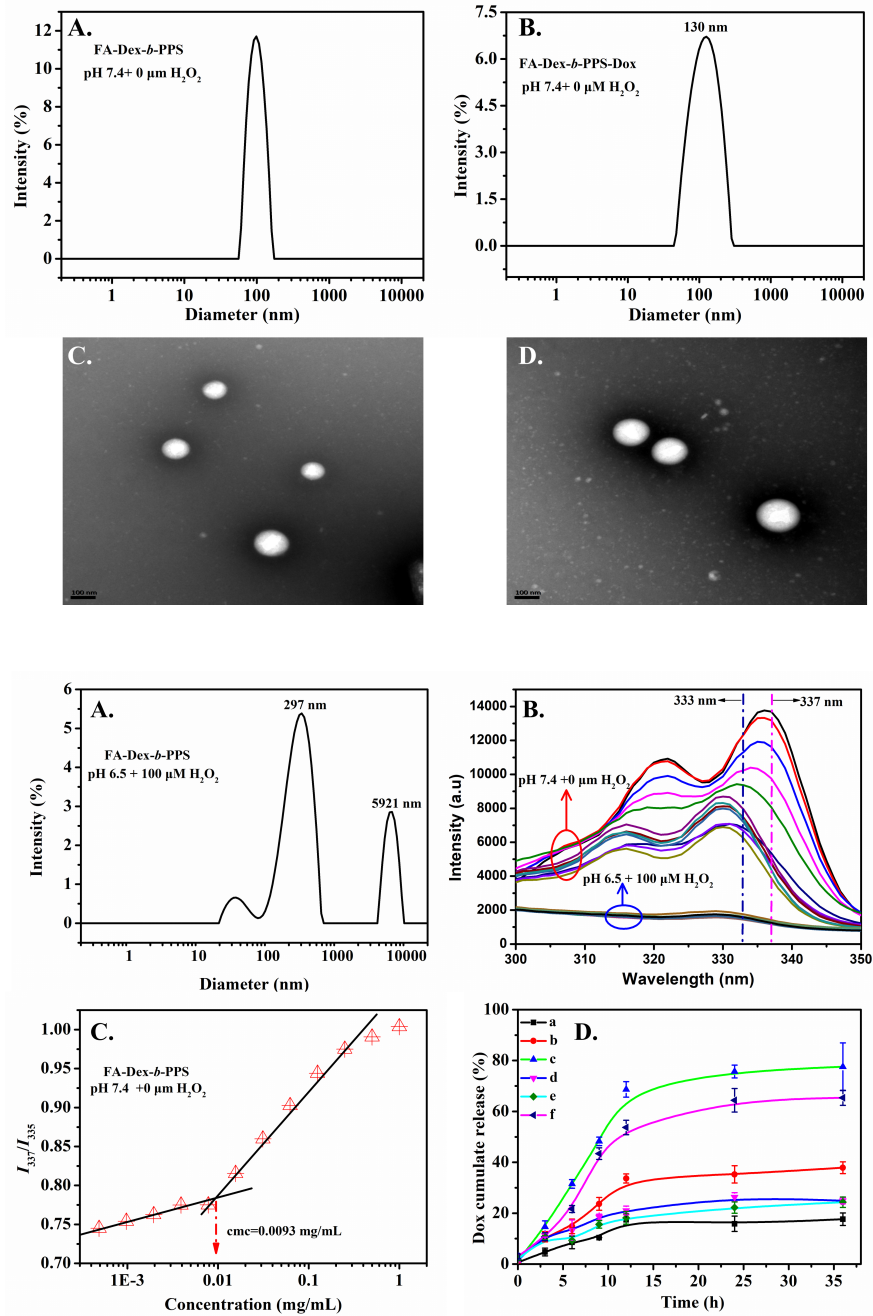
³Nanfang Hospital, Southern Medical University

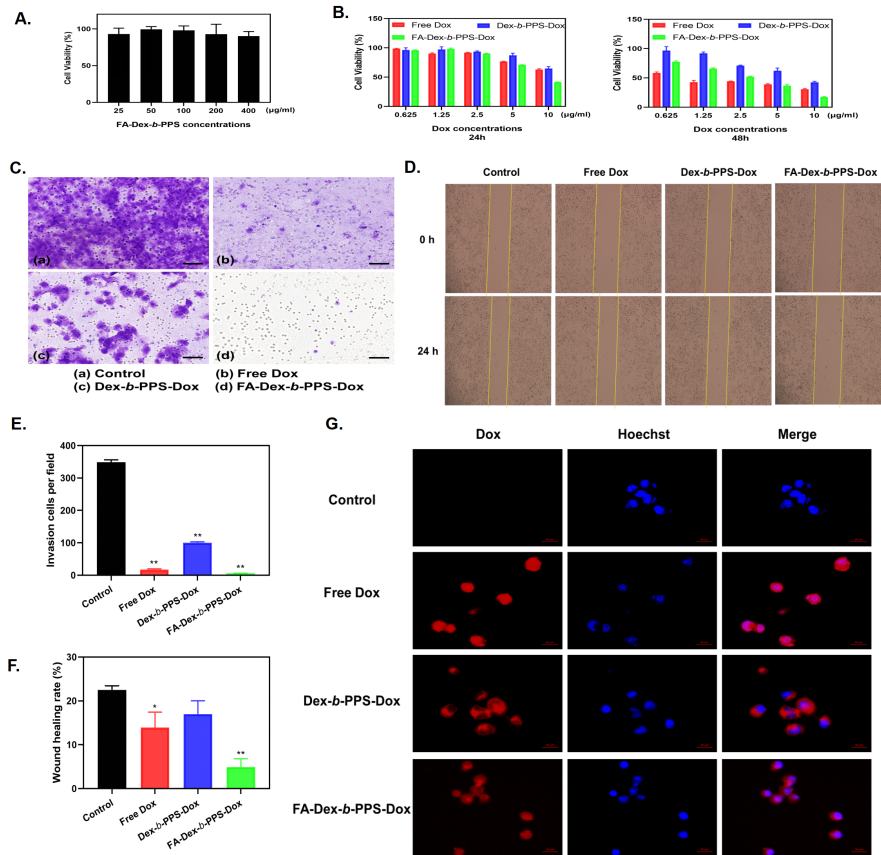
⁴Affiliation not available

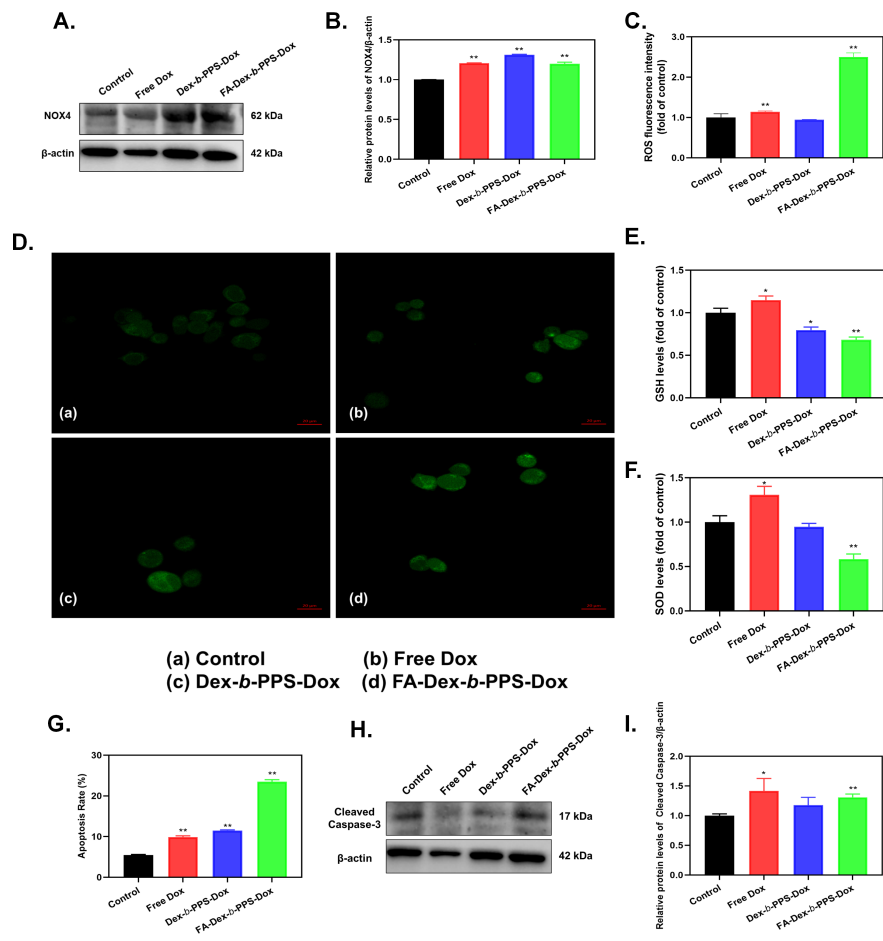
September 02, 2024

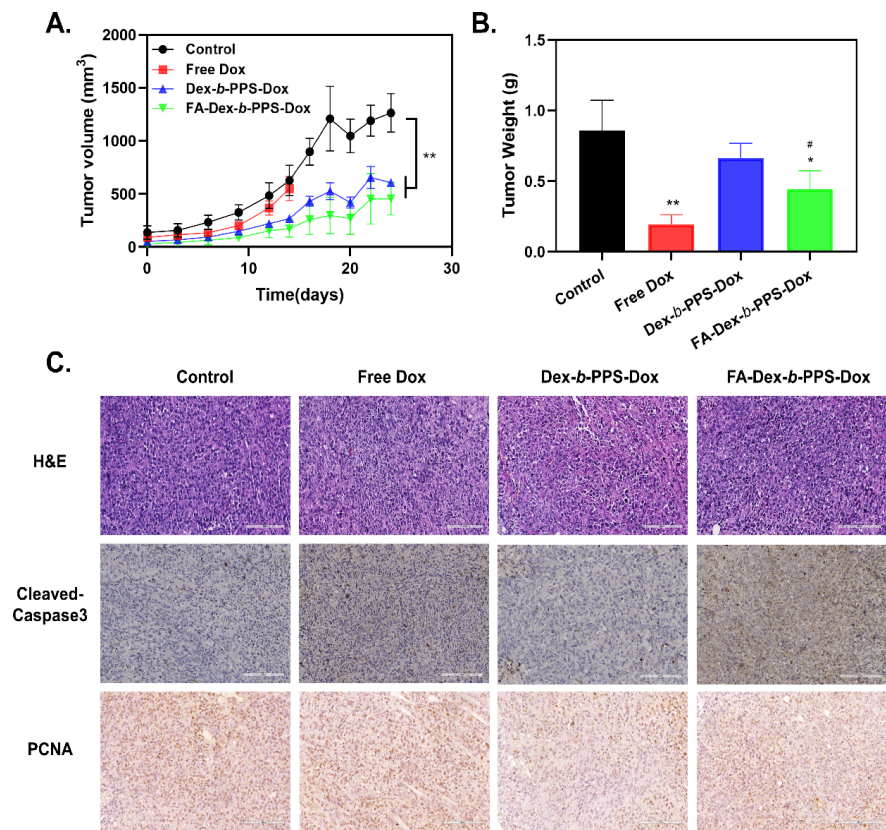
Abstract

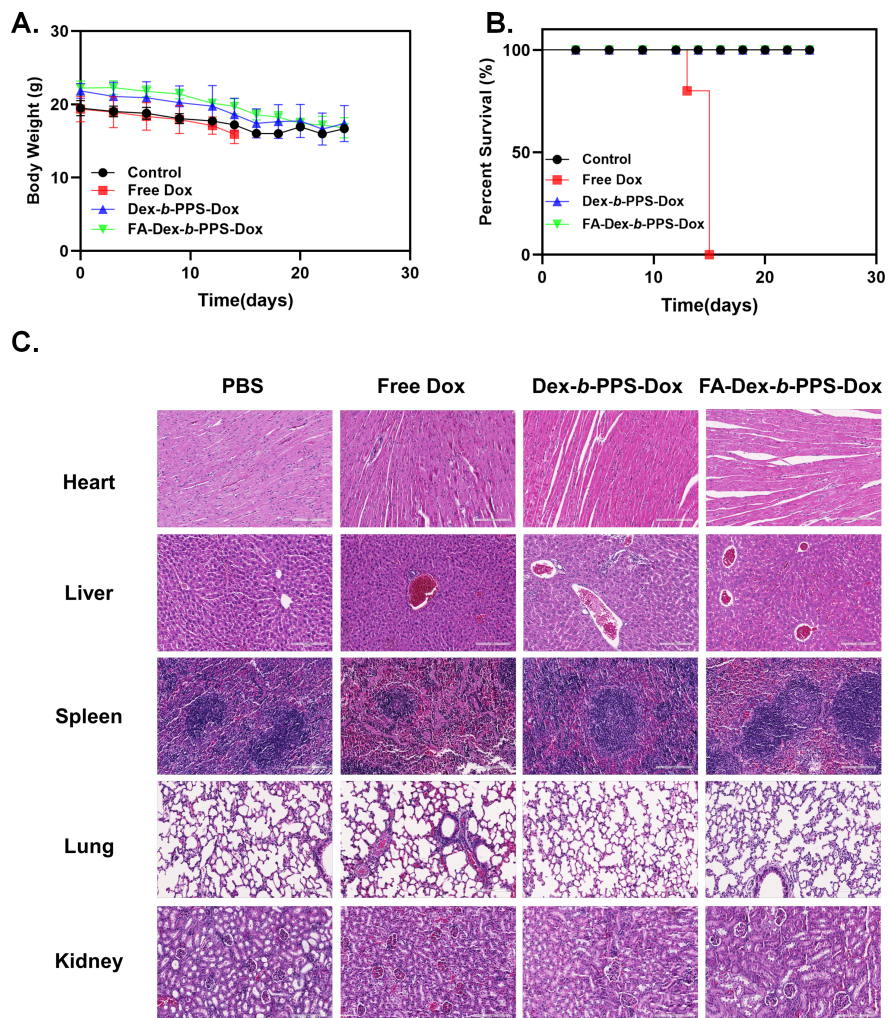
This study presents a novel approach in nanomedicine for targeted cancer therapy by leveraging folic acid-receptor (FR) interactions and reactive oxygen species (ROS)-responsive nanocarriers. Utilizing big data to advance nanomedicine, we developed an innovative amphiphilic conjugate, folic acid (FA) decorated dextran-block-poly copolymer (FA-Dex-b-PPS), designed to serve as ROS-responsive nanocarriers specifically for prostate cancer treatment. The chemical structure of FA-Dex-b-PPS was confirmed via Fourier transform infrared spectroscopy and proton nuclear magnetic resonance. The self-assembly into ROS-responsive nanoparticles and subsequent degradation were characterized through fluorescence spectroscopy, dynamic light scattering, and transmission electron microscopy. Therapeutic nanocarriers encapsulating doxorubicin (Dox) were prepared via dialysis, demonstrating efficient oxidant-triggered Dox release *in vitro*. Cytotoxicity assays revealed high biocompatibility, with cell survival rates exceeding 85% at 400 $\mu\text{g}/\text{mL}$. Confocal laser scanning microscopy confirmed the efficient internalization of FA-Dex-b-PPS-Dox nanoparticles by PC3 cells via FR-mediated endocytosis, surpassing non-targeted Dex-b-PPS-Dox nanoparticles. Furthermore, *in vitro* and *in vivo* xenograft mouse model analyses consistently demonstrated that FA-Dex-b-PPS-Dox nanoparticles exhibited superior anti-tumor efficacy against PC3 cells compared to non-targeted and free Dox counterparts. These findings underscore the potential of tumor-targeted, ROS-responsive nanocarriers in enhancing the efficacy of cancer therapy.











1 **Folate Receptor-Targeted, ROS-Responsive Dextran-Block-Poly**
2 **(propylene sulfide) Copolymer Nanoparticles: A**
3 **Bioinformatics-Guided Approach for Prostate Cancer Therapy**

4 Yixun Zhang^{b,1}, Zhenguo Liang^{d,1}, Zeheng Tan^{g,1}, Jundong Lin^{d,e,1}, Xinqing Jiang^a,
5 Ruimeng Yang^a, Jian Zhang^{c,d}, Huijing Tan^{c,d}, Wenjie Xie^c, Yangjia Zhuo^c, Fen Zou^c,
6 Jianheng Ye^c, Jianming Lu^c, Yingke Liang^c, Ronghua Yang^{b,*}, Weide Zhong^{c,d,e,f,*},
7 Huikang Yang^{a,*}.

8 a, Department of Radiology, the Second Affiliated Hospital, School of Medicine,
9 South China University of Technology, Guangzhou, Guangdong, China

10 b, Department of Burn and Plastic Surgery, the Second Affiliated Hospital, School of
11 Medicine, South China University of Technology, Guangzhou, Guangdong, China

12 c, Department of Urology, the Second Affiliated Hospital, School of Medicine, South
13 China University of Technology, Guangzhou, Guangdong, China

14 d, Guangdong Provincial Key Laboratory of Urology, the First Affiliated Hospital of
15 Guangzhou Medical University, Guangzhou Medical University, 510230,
16 Guangzhou, Guangdong, China.

17 e, Guangzhou Laboratory, No. 9 XingDaoHuanBei Road, Guangzhou International
18 Bio Island, Guangzhou 510005, Guangdong, China

19 f, State Key Laboratory of Quality Research in Chinese Medicine, Macau University
20 of Science and Technology, Taipa, 999078 Macau, China

21 g, Guangdong Provincial Institute of Nephrology, Nanfang Hospital, Southern
22 Medical University, Guangzhou, 510515, China

23 * To whom correspondences should be addressed: E-mail: 21720091@qq.com,
24 zhongwd2009@live.cn; eyyanghk@scut.edu.cn.

25 ¹ These authors contributed equally to this work.

26

27 **ABSTRACT**

28 Utilizing big data to advance nanomedicine, especially via folic acid-receptor (FR)
29 interactions for targeted cancer treatment, underscores a novel approach in oncology.
30 Reactive oxygen species (ROS)-responsive nanocarriers, in particular, can rapidly
31 release drugs in response to ROS stimulation, making them highly effective for tumor
32 therapy. In this study, we fabricated a novel amphiphilic conjugate composed of folic
33 acid (FA) decorated dextran-block-poly copolymer (FA-Dex-*b*-PPS) to serve as
34 ROS-responsive nanocarriers for the treatment of prostate cancer. The chemical
35 structure of FA-Dex-*b*-PPS was confirmed using Fourier transform infrared
36 spectroscopy and proton nuclear magnetic resonance. The self-assembling behavior of
37 FA-Dex-*b*-PPS into ROS-responsive nanoparticles and their degradation was
38 characterized using fluorescence spectroscopy, dynamic light scattering, and
39 transmission electron microscopy. Therapeutic nanocarriers encapsulating
40 doxorubicin (Dox) were formed via dialysis. The FA-Dex-*b*-PPS nanoparticles
41 demonstrated excellent oxidant-triggered Dox release ability *in vitro*. The outcomes
42 from the cytotoxicity assays indicate that the FA-Dex-*b*-PPS nanocarriers exhibit high
43 biocompatibility, with cell survival rates exceeding 85 % even at concentrations of
44 400 µg/mL. The utilization of confocal laser scanning microscopy for analysis
45 demonstrated that the FA-Dex-*b*-PPS-Dox nanoparticles were efficiently internalized
46 by PC3 cells through FR, in contrast to the non-FA coated drug-containing
47 nanoparticles (Dex-*b*-PPS-Dox). Furthermore, both *in vitro* and *in vivo* xenograft
48 mouse model analyses consistently demonstrated that FA-Dex-*b*-PPS-Dox
49 nanoparticles exhibited the best anti-tumor effect toward PC3 cells compared to
50 non-targeted Dex-*b*-PPS-Dox nanoparticles and free Dox at the same Dox dosage.
51 These combined data suggest that nanocarriers with tumor-targeting capabilities and
52 ROS response have greater potential for application in tumor therapy.

53 **1. Introduction**

54 Cancer ranks as a predominant factor contributing to mortality worldwide[1] .
55 Prostate cancer (PCa) is frequently diagnosed among men across various cancer types,

56 characterized by high recurrence, metastatic rates, and mortalities. Effective therapies
57 for PCa remain an unmet clinical need. Consequently, identifying targeted therapeutic
58 approaches has become one of the pressing challenges in current clinical medical
59 research. By deeply analyzing the pathogenesis and clinical characteristics of PCa,
60 researchers are striving to explore novel therapeutic strategies and methods to
61 enhance treatment efficacy and improve patient prognosis[2]. Concurrently, the
62 advancement of science and technology has introduced emerging treatment modalities
63 and techniques, offering new hope and possibilities for PCa therapy[3].

64 Conventional chemotherapy is one of the treatments for PCa; however, the
65 clinical application of chemotherapeutic agents is constrained by their limited water
66 solubility, absence of specificity, and elevated toxicity[4]. In order to surmount these
67 challenges, scientists have engineered advanced drug delivery platforms including
68 liposomes, hydrogels, and exosomes, with nanomedicine at the forefront of this
69 research area[5]. Extensive research has been conducted on polymeric nanoparticles
70 owing to their desirable attributes, which include biocompatibility, stability, and a
71 substantial drug-loading capacity[6]. Unfortunately, most polymeric drug carriers lack
72 the ability to actively target tumors and release drugs rapidly, which reduces the
73 effectiveness of chemotherapy. Consequently, there exists an urgent requirement to
74 engineer sophisticated polymeric nanoparticles that possess both tumor-targeting and
75 rapid drug release functionalities for the treatment of PCa.

76 With the rapid development of big data analysis technologies, integrating these
77 technologies to advance nanomedicine research has become a new trend in medical
78 research[7]. Specifically, the specific interactions between folic acid (FA) and its
79 receptors have recently become a focal point in academic research on targeted
80 delivery of nanomedicines. FOLH1, also known as FA, is a gene that encodes a type
81 II transmembrane glycoprotein of the M28 peptidase family. FA is a crucial molecule
82 involved in several biological processes, such as RNA and DNA preparation,
83 methylation, and modification. FA serves as the principal binding agent to the FR, a
84 protein that is excessively expressed in the majority of cancerous cells[8, 9]. The

85 specific binding of FA and the folic acid receptor has been utilized as the basis for
86 many targeted therapies to achieve precise drug delivery[10]. For example,
87 FA-modified poly(ϵ -caprolactone) block poly(2-methacryloxyethyl phosphorylcholine)
88 copolymers have shown higher cellular uptake compared to non-FA-modified
89 counterparts in some cancer cells[11]. Moreover, studies have documented that the
90 modification of FA-DABA-SMA copolymers is capable of decreasing the expression
91 of HES1 and NOTCH1 proteins, thereby enhancing the levels of FR α expression in
92 breast cancer cells[12]. In recent years, researchers have utilized FA conjugation to
93 nanoparticles to achieve targeted cancer therapy. For instance, mixed miRNAs-loaded
94 FR-conjugated PLGA nanoparticles have been designed to eliminate cancer cells from
95 spermatogonia stem cells[13]. Similarly, Dox-conjugated glycol-block copolymer
96 coated multiwall carbon nanotubes decorated with FR have been used to enrich Dox
97 accumulation in tumor tissue and achieve targeted therapy of breast cancer[14]. In
98 summary, the conjugation of FA has demonstrated potential in facilitating targeted
99 drug delivery for the treatment of cancer. The exploitation of the interaction between
100 FA and its receptor for targeted therapeutic approaches holds significant promise for
101 the advancement of future strategies in cancer treatment. However, current research
102 on the application of clinical data analysis in the bioinformatics study of FA in
103 pan-cancer or PCa is still inadequate. Moreover, there is a notable lack of
104 nanomedicine designed and constructed based on bioinformatics analysis results for
105 the targeted treatment of PCa.

106 In recent years, the domain of pharmaceuticals and biomedicine has witnessed a
107 growing trend in the development of smart drug delivery systems that respond to
108 various stimuli[15]. Researchers have designed and synthesized a variety of
109 stimuli-responsive polymeric nanoparticles to achieve targeted release of
110 chemotherapy drugs and improve the antitumor effect, based on the characteristics of
111 tumor tissue such as temperature, pH, ultrasound, reactive oxygen species (ROS), and
112 enzyme stimulation[16, 17]. It is well known that ROS, including H₂O₂, superoxide,
113 hydroxyl radical, and others, are highly expressed in cancer cells. ROS-responsive

114 polymeric nanoparticles, as drug delivery systems, have developed as an effective
115 strategy for precise therapy, based on the higher ROS concentration in tumor tissues
116 compared with normal tissues[18-20]. Drug delivery from ROS-responsive polymeric
117 nanoparticles occurs mainly through two different pathways, namely,
118 hydrophobic-hydrophilic transition and the degradation of polymeric chain
119 segments[21, 22]. On one hand, ROS can oxidize hydrophobic polymers, which have
120 chalcogen elements (such as S, Se, Te) in their backbone or side chain, into
121 hydrophilic polymers. This hydrophobic-hydrophilic transition leads to dissociation of
122 the polymer self-assembly and ultimately results in the rapid release of the drug. On
123 the other hand, ROS-sensitive chemical structures, such as boronic acid esters, proline
124 oligomers, thioketal, or diselenide groups, can be introduced into the polymer
125 structure. The presence of ROS can then degrade the polymer, enabling rapid release
126 of the drug. Therefore, ROS-responsive polymeric nanoparticles have great potential
127 as drug delivery platforms in the future.

128 Polypropylene sulfide (PPS) is regarded as an ideal ROS-responsive polymer.
129 The rationale for this lies in the facile synthesis of PPS through an anion-initiated
130 ring-opening polymerization of propylene sulfide. Additionally, under the influence of
131 ROS, the hydrophobic sulfur atoms within the PPS backbone can undergo oxidation,
132 transitioning into hydrophilic sulfoxide or sulfone groups[23, 24]. This allows the
133 polymer to undergo a hydrophobic-hydrophilic transition for rapid and controlled
134 release of the drug[25]. Currently, polyethylene glycol-block-polypropylene sulfide
135 (PEG-*b*-PPS) amphiphilic block copolymers are widely used as ROS-sensitive
136 nanocarriers for the treatment of tumors, inflammation, and other diseases[26, 27].
137 This is mainly due to the fact that PEG is already approved by the FDA for improving
138 the pharmacokinetics and bioavailability of drugs[28]. In addition, PEG-*b*-PPS can be
139 easily synthesized by an anionic ring-opening polymerization reaction using PEG as a
140 macromolecular initiator[29]. Nonetheless, it is important to acknowledge that
141 polyethylene glycol (PEG) is a non-biodegradable biomaterial, and the existence of
142 anti-PEG antibodies in patients treated with PEG-conjugated pharmaceuticals could

143 potentially diminish the therapeutic efficacy[30, 31]. Furthermore, the lack of
144 functional groups on the PEG segment makes it difficult to introduce targeting ligands
145 on PEG-*b*-PPS. Overall, PEG-*b*-PPS amphiphilic block copolymers remain a
146 promising platform for drug delivery. Nevertheless, further research is required to
147 address the limitations of PEG and optimize their performance for specific
148 applications.

149 Renewable and biodegradable natural polysaccharides, including starch, dextran,
150 hyaluronic acid, and cellulose, have attracted substantial interest due to their potential
151 utility in the biomedical field[32]. Dextran stands out as a polysaccharide of choice
152 for in-depth exploration, largely due to its desirable characteristics including aqueous
153 solubility, compatibility with biological systems, and a reduced potential to elicit an
154 immune response[33]. While dextran-based block polymers have not been extensively
155 studied, recent literature reports have focused on the preparation of
156 dextran-containing amphiphilic block polymers using click reactions[34, 35]. This
157 method offers meticulous regulation of the material's architecture and attributes,
158 enabling the integration of dextran's benefits with those of other substances. Moreover,
159 the hydroxyl groups on the dextran allow for further modifications by coupling
160 various targeting ligands, fluorescent molecules, and drugs[36-38]. Despite the
161 promising applications of dextran-based block polymers, there is currently no
162 research on dextran-block-polypropylene sulfide copolymers. This is an exciting area
163 of potential research, as polypropylene sulfide is another biodegradable material that
164 exhibits favorable properties for biomedical applications.

165 In this study, we initially extracted the expression data of FA across 33 pan-cancer
166 types from the publicly available repository, The Cancer Genome Atlas (TCGA).
167 Thereafter, we analyzed the role of FA in tumor cell stemness. Progressing from this,
168 our study explored the relationship between FA and PCa in terms of TNM staging,
169 prognostic survival, and tumor infiltrating immune cells. Building on the critical
170 theoretical foundation of FA's high expression in PCa, we report the synthesis of FA
171 decorated dextran-block-polypropylene sulfide polymer using click chemistry and

172 EDCI/HOBT-catalyzed esterification reactions. The obtained amphiphilic polymer's
173 chemical structure was characterized using Fourier transform infrared spectroscopy
174 (FTIR) and nuclear magnetic resonance (NMR). Furthermore, the self-assembly
175 behavior of the amphiphilic block polymer was demonstrated using dynamic light
176 scattering (DLS), transmission electron microscopy (TEM), and fluorescence
177 spectroscopy. Additionally, Dox-loaded FA-Dex-*b*-PPS nanoparticles were found to
178 exhibit ROS-responsive drug release behavior under high ROS environments
179 (Scheme 1). *In vitro* and *in vivo* experiments were conducted to compare the
180 anti-tumor effect of FA-Dex-*b*-PPS-Dox nanoparticles, non-targeted Dex-*b*-PPS-Dox
181 nanoparticles, and Free Dox, all at the same Dox dosage. The results demonstrated
182 that FA-Dex-*b*-PPS-Dox nanoparticles exhibited the best anti-tumor growth effect
183 towards PC3 cells. Drawing from both *in vitro* and *in vivo* experimental outcomes, we
184 observed that employing FA as a tumor-targeting ligand can augment the intracellular
185 drug concentration and potentiate the antitumor efficacy of Dox-loaded nanoparticles.

186 **2. RESULTS AND DISCUSSION**

187 **2.1 Pan-Cancer Analysis of FOLH1 Transcriptomic Expression and Its** 188 **Correlation with Tumor Stemness and Prostate Cancer Pathology**

189 To thoroughly investigate the transcriptomic expression pattern of FOLH1 across
190 various cancers, we utilized pan-cancer data encompassing 34 common cancer types
191 from the TCGA database. As depicted in Figure 1A, FOLH1 expression was found to
192 be significantly altered in multiple cancer types, such as UCEC, LUAD, ESCA, STES,
193 KIPAN, COAD, COADREAD, PCPG, PRAD, KIRC, LUSC, THCA, OV, PAAD,
194 UCS, LAML, GBM, GBMLGG, LGG, BRCA, KIRP, STAD, LIHC, WT, SKCM,
195 KICH, and CHOL. These findings underscore the pivotal role of FOLH1 in cancer
196 pathogenesis (all P values <0.05). Then, to investigate the role of the FOLH1 gene in
197 tumor stemness, we calculated the Spearman correlation between FOLH1 gene
198 expression and tumor stemness scores within each cancer type. As depicted in Figure
199 1B, significant correlations were observed in 18 cancer types, with 4 of these
200 demonstrating a significant positive correlation. These included

201 BRCA(N=1080)(R=0.148942256393485,P=8.80956467409179e-7),PRAD(N=491)(R
202 =0.258044667531986,P=6.55838181611533e-9),LUSC(N=483)(R=0.2065064681831
203 96,P=0.0000047371602794732),ACC(N=76)(R=0.289905397385117,P=0.011077122
204 6466697). In contrast, a significant negative correlation between FOLH1 gene
205 expression and tumor stemness scores was found in 14 other cancer types, such as
206 LGG(N=507)(R=-0.123664750206764, P=0.00529765414468569) ,
207 CESC(N=301)(R=-0.19327883282091, P=0.000748542829133704),
208 COAD(N=281)(R=-0.314768065937981, P=7.02241656987141e-8),
209 COADREAD(N=369)(R=-0.280195437770192, P=4.3960481873053e-8),
210 SARC(N=253)(R=-0.153905971298841, P=0.014460193903918) ,
211 KIPAN(N=860)(R=-0.589272769954414, P=1.55736718515943e-81) ,
212 UCEC(N=177)(R=-0.265404997445562, P=0.000356694282028656) ,
213 KIRC(N=512)(R=-0.407254021627045, P=7.08589079849258e-22),
214 THYM(N=119)(R=-0.264175478120932, P=0.00369422930699814). These findings
215 provide crucial insights for further exploration of the mechanism by which the
216 FOLH1 gene influences tumor stemness. It is evident that FOLH1 is highly expressed
217 in prostate cancer, rendering it a promising target for future investigative research.

218 In light of the above bioinformatics analysis of FOLH1 across pan-cancer
219 datasets and drawing upon the foundation of our previous research efforts, we have
220 chosen PCa as the tumor type for our subsequent studies. The relationship between
221 FOLH1 and pathologic T stage, pathologic N stage, clinical M stage from
222 TCGA-PRAD dataset were further analyzed. As illustrated in Figures 1C and 1D, PCa
223 patients with high levels of FOLH1 expression are correlated with more severe
224 pathological T stages (T3 and T4) and elevated pathological N stages (N1). However,
225 there was no significant association between FOLH1 expression status in clinical M
226 stage (Figure 1E). The area under the receiver operating characteristic (ROC) curve
227 (AUC) for FOLH1 reached 0.828 (Figure 1F), signifying that FOLH1 expression
228 possesses considerable diagnostic utility in the context of PCa.

229 The collective bioinformatics findings indicate that the strategic design of

230 nanomedicines targeting FOLH1 harbors significant potential for therapeutic
231 advancement. FOLH1, also known as the folate receptor, has been the subject of
232 numerous studies wherein folate-conjugated nanotherapeutics have been employed to
233 target tumor cells expressing the folate receptor, thereby facilitating precision-targeted
234 therapy.

235 **2.2 Preparation and Characterization of FA-Dex-*b*-PPS**

236 The number of polysaccharide-based block polymers is significantly lower when
237 compared to polyethylene glycol-based block polymers. This is mainly due to the
238 large number of reactive groups on the polysaccharides need to protect, the lower
239 activity of the terminal reducing groups and difficult to find good solvent for both
240 blocks that limit the preparation of polysaccharide-based block polymers[39].
241 Currently, chemical conjugation is widely used to synthesis polysaccharide-based
242 block polymers. However, the reaction efficiency of coupling reactions between two
243 large molecular blocks is usually low. Therefore, coupling reactions with high
244 efficiency and selectivity are the basic requirements for the preparation of
245 polysaccharide-based block polymers. Cu(I)-catalyzed "alkyl/azide" click reactions
246 occurring under mild reaction conditions are highly selective, efficient, and reliable
247 and play a crucial role in the preparation of polysaccharide block polymers[35]. In
248 this study, dextran/poly(propylene sulphide) block polymer was prepared by using the
249 Cu(I)-catalyzed "alkyl/azide" click reactions. To achieve this, α -azide-dextran was
250 synthesized using the reductive amine reaction and α -alkyl-PPS was synthesized
251 through anionic ring-opening polymerization. The dextran/poly(propylene sulphide)
252 amphiphilic block polymer was then prepared by click reaction. Finally, folic acid
253 molecule was grafted onto the dextran chain segment by esterification to enable the
254 block polymer the ability to target the folic acid receptor, as shown in Scheme 2.

255 The chemical structure of the polymers was characterized by infrared
256 spectroscopy, as illustrated in Figure 2A. For the α -azide Dex, the stretching vibration
257 absorption peak of the hydroxyl group on the polysaccharide was located at 3500 cm^{-1} ,
258 and the characteristic peak of the azide group appeared at 2106 cm^{-1} . This indicated

259 that the azide group was successfully introduced to the reducing-end of the dextran
260 via the reductive amine reaction. The C-H stretching vibration of PPS was observed in
261 the region of 2850-3000 cm^{-1} . The spectrum for FA-Dex-*b*-PPS clearly showed that
262 the azide group absorption peak at 2106 cm^{-1} had completely disappeared, indicating
263 that the product was successfully prepared through the click reaction. Furthermore,
264 the hydroxyl absorption peak on the dextran chain segment appeared at 3500 cm^{-1} and
265 the absorption peak located at 1430 cm^{-1} was attributed to PPS block.

266 The molecular structure of α -alkyne-PPS was elucidated using NMR
267 spectroscopy, with the resulting data depicted in Figure 2B. The chemical shift of the
268 H-atom of the methyl group on the initiator n-butyl mercaptan was located at 0.90
269 ppm. The peak attributed to the methyl groups of the propylene sulphide repeated
270 units appeared at 1.35 ppm, and the H-atom attributed to the methylene group was
271 located at 2.52-2.65 ppm. The peak located at 2.85-3.00 ppm belonged to the
272 hypomethyl group. By comparing the integrated area of the methyl group on the
273 repeat unit of PPS with that of the initiator methyl group, we were able to calculate
274 the polymerization degree of PPS to be approximately 78, and the molecular weight to
275 be approximately 5911 g/mol, which was calculated based on the following equation:
276 $M_{\text{1-buthane thiol}} + M_{\text{propylene sulfide}} \times 78 + M_{\text{Propargyl bromide}} - M_{\text{HBr}} = 90.19 \text{ g/mol} + 74.14$
277 $\text{g/mol} \times 78 + 118.96 \text{ g/mol} - 80.91 \text{ g/mol} = 5911 \text{ g/mol}$ (3), where M represents the
278 molar mass.

279 We employed NMR spectroscopy to determine the detailed chemical structure
280 of the dextran/poly(propylene sulphide) block polymer synthesized via the click
281 reaction in DMSO. As exhibited in Figure 2C, all the H-atom peaks attributed to
282 dextran and PPS blocks were identified. Moreover, the H-atom on the triazole ring
283 which was produced after the click reaction was located at 8.10 ppm. The presence of
284 the triazole ring provided compelling evidence for the successful preparation of
285 dextran/poly(propylene sulphide). Using the ratio between the integrated area of the
286 methyl H-atom signal of PPS and the methyl H-atom of dextran, we calculate that the
287 molar ratio of the hydrophobic and hydrophilic repeating units in the polymer is about

288 2.22:1, which corresponded to a mass fraction of hydrophobic chain segments of
289 approximately 50 %. We cannot provide GPC data for dextran/poly(propylene
290 sulphide) mainly due to the block copolymer can only be dissolved in DMSO,
291 however, we do not have a GPC with DMSO as the mobile phase.

292 The folic acid molecule was grafted onto the dextran block via the
293 EDCI/HOBT-catalyzed esterification. Since folic acid contains unsaturated structures
294 such as benzene rings, the H on this type of unsaturated structure appears at high
295 chemical shifts. As shown in Figure 2D, the characteristic peaks of unsaturated cyclic
296 structures on folic acid were appeared at 6.50-8.50 ppm, confirming the successful
297 synthesis of target product. The degree of substitution of folic acid was calculated
298 from the NMR spectra as approximately 1.7 folic acid molecules per dextran block by
299 the ratio of the integrated area of the H-atom signal of the benzene ring on the folic
300 acid to the integrated area of the methyl H-atom signal on the n-butyl mercaptan.

301 **2.3 Preparation and characterization of ROS sensitive-nanoparticles**

302 The FA-Dex-*b*-PPS block polymer composed of hydrophilic dextran block and
303 hydrophobic PPS block, allowing it to self-assembly into nanoparticles in selective
304 solvents. In this study, FA-Dex-*b*-PPS based nanoparticles were obtained through a
305 nanoprecipitation process. It's well known that the size of nanoparticles plays an
306 important role in drug delivery, as it determines whether the drug can reach the tumor
307 site by passthrough the biological barriers and escaping clearance by the immune
308 system during *in vivo* circulation[40]. Figure 3A shows the DLS result of the blank
309 nanoparticles in aqueous solution. The size of the nanoparticles was approximately
310 101 nm when the nanoparticles were dispersed at a pH=7.4 aqueous solution
311 mimicked the human physiological environment and in the absence of H₂O₂. The
312 morphology of the nanoparticles was observed by transmission electron microscopy
313 (TEM). As shown in Figure 3C, the nanoparticles were spherical in structure.
314 Subsequent, we investigated the particle size and morphology of nanoparticles after
315 encapsulated with the hydrophobic antitumor drug Dox. From Figure 3B, we could
316 find that after loading with hydrophobic drug, the particle size of the nanoparticles

317 was increased from 101 nm to 130 nm. This is mainly due to the encapsulation of
318 hydrophobic drug in the hydrophobic core of the nanoparticles through hydrophobic
319 interaction[41]. As Figure 3D shows that the drug-loaded nanoparticles maintained
320 their spherical like morphology, and exhibited a larger size than the blank
321 nanoparticles.

322 The stability of nanoparticles is crucial in *in vivo* drug delivery since it prevents
323 drug premature release, extends circulation time of drug in the blood vessel, and
324 enhances drug accumulation at the tumor site[42]. Critical micelle concentration is a
325 widely used parameter to characterized the stability of nanoparticles. Pyrene can act
326 as fluorescent probe to measure the cmc value. Figure 4C shows the fluorescence
327 spectroscopy of pyrene at different polymer concentrations at pH 7.4 and 0 μM H_2O_2 .
328 As the polymer concentration increases, a noticeable red-shift in the fluorescence
329 spectroscopy of pyrene was occurs. This phenomenon is due to the gradual formation
330 of nanoparticles with hydrophobic cores as the polymer concentration increases. The
331 hydrophobic pyrene is encapsulated within the hydrophobic cores of the nanoparticles
332 through physical interactions, causing a change in their chemical environment and
333 resulting in a red-shift in their fluorescence spectra[43]. The cmc value of
334 FA-Dex-*b*-PPS was approximately 0.0093 mg/mL, calculated from I_{337}/I_{335} versus the
335 logarithm of the concentration (Figure 4C). However, when the polymeric
336 nanoparticle in a solution with pH 6.5 and 100 μM H_2O_2 , the amphiphilic polymer
337 was oxidized to a fully hydrophilic polymer. Consequently, even though the polymer
338 concentration increase, it is impossible to form nanoparticles. The fluorescence
339 spectra of pyrene at different polymer concentrations under these conditions (Figure
340 4B) indicate that the fluorescence intensity of pyrene is weak, and there is no red-shift
341 in the spectra. As a result, the cmc value cannot be obtained.

342 **2.4 Drug loading and ROS triggered *in vitro* release**

343 Doxorubicin is a broad-spectrum chemotherapeutic agent; however, its therapeutic
344 utility is compromised by its poor aqueous solubility and the occurrence of
345 toxicological effects on non-targeted organs. Amphiphilic block polymers are widely

346 used as drug nanocarriers to enhance the water solubility of antitumor drugs and
347 minimize their side effects. In this study, Dox was encapsulated within the
348 hydrophobic core of FA-Dex-*b*-PSS nanoparticles using a nano-precipitation method.
349 The drug loading content was approximately 6.3 %, indicating the potential of
350 FA-Dex-*b*-PSS as a promising nano-drug delivery system for tumor therapy.

351 Further, the release of the encapsulated drug from the drug-laden nanoparticles was
352 investigated *in vitro*. As shown in Figure 4D, under normal physiological conditions
353 (pH=7.4, 0.0 μM H_2O_2), Dox was slowly released from the nanoparticles, and the
354 cumulative release was no more than 20 % over 72 h. At a weak acid environment
355 (pH=6.5, without H_2O_2), the release rate of Dox increased slightly, and the cumulative
356 release of approximately 30 % at the same period. A faster drug release rate was
357 observed under a pH=4.5 acidic conditions (without H_2O_2), and almost 70 % of the
358 Dox was released over 72 h. This phenomenon could be attributed to the improved
359 solubility of Dox under acidic conditions[44]. Under simulate human physiological
360 conditions (pH 7.4 contain with 100 μM H_2O_2), the cumulative 72 h release of Dox
361 was less than 20 %. Maintaining the same pH of 7.4 and increase the H_2O_2
362 concentration to 500 μM did not significantly increase the release of Dox, with the
363 cumulative drug release only approaching 28 %. This indicated that PPS could not be
364 oxidized only in the presence of H_2O_2 . However, when the pH value was lowered to
365 6.5 and H_2O_2 concentration was set at 100 μM , approximately 60 % of the Dox was
366 released from the nanoparticles. As mentioned above, the PPS block could be
367 oxidized under weak acidic conditions, containing 100 μM H_2O_2 , resulting in a
368 hydrophobic to hydrophilic transition. Hence, under this condition, a faster release of
369 Dox phenomenon could be observed.

370 **2.5 The antitumor effects of FA-Dex-*b*-PPS-Dox and cellular uptake on prostate** 371 **cancer cells in vitro**

372 It has also been reported that targeted therapy of prostate cancer can be achieved
373 by targeting PC3 cells with folic acid decorated nanoparticles[45, 46]. These results
374 suggest that we can achieve prostate cancer precise therapy by targeting folate

375 receptor of PC3 cells. Hence, PC3 cells were selected as our research cells in this
376 study based on the above basis. Firstly, the biocompatibility of the synthesized
377 FA-Dex-*b*-PPS was evaluated by CCK-8 assay in vitro. When the concentration of
378 FA-Dex-*b*-PPS reached 400 $\mu\text{g/mL}$, the PC3 cells survival rate was still more than
379 80 %, indicating there was good biocompatibility of FA-Dex-*b*-PPS as nanocarriers
380 (Figure 5A). Then, after FA-Dex-*b*-PPS encapsulating with Dox, we quantified it with
381 Dox as the gradient concentration to evaluate the inhibition of cell proliferation by
382 CCK-8 assay. After 24 h incubation, the cell viability of FA-Dex-*b*-PPS-Dox group
383 was 41.46 ± 0.31 % compared with the control group, while cell viability dropped to
384 only 17.61 ± 0.47 % after 48 h incubation. FA-Dex-*b*-PPS-Dox inhibited the growth
385 of PC3 cells more obviously than Free Dox and Dex-*b*-PPS-Dox (Fig. 5B).
386 Furthermore, the invasion and migration with different treatment on PC3 cells were
387 also evaluated by transwell and wound healing assays. As shown in Figure 5C, 5D, 5E,
388 and 5F, different treatments could inhibit the invasion and migration on PC3 cells.
389 FA-Dex-*b*-PPS-Dox exhibited great stronger inhibition both invasion and migration
390 among them.

391 Next, to visualize distribution of the nanoparticles, PC3 cells were incubated with
392 5 $\mu\text{g/mL}$ Dox of nanoparticles for predetermined time durations. Then specificity and
393 cellular accumulation of Free Dox or nanoparticles by PC3 cell lines were confirmed
394 by confocal laser scanning microscopy (CLSM) through intracellular Dox
395 accumulations (red-fluorescence) (Figure 5G). The cell nuclei were labeled with
396 Hoechst dye, exhibiting a blue fluorescence. Notably, following incubation, the free
397 form of Dox preferentially accumulated within the cell nuclei, having been
398 transported into the cells via osmosis. This is consistent with previous literature
399 reports that the uptake of Dox was mainly dependent on a diffusion mechanism[47].
400 Compared with Free Dox, it is of more accumulation of Dex-*b*-PPS-Dox
401 nanoparticles in cytoplasm. While FA-Dex-*b*-PPS-Dox distributed diffusely both cell
402 nuclei and cytoplasm of cells, which was speculated to the uptake of Dox through the
403 folic acid receptor-mediated endocytosis process, leading to its uniform distribution in

404 the whole cell[48]. All the above results demonstrates that FA-Dex-*b*-PPS-Dox has a
405 good antitumor effect *in vitro* and is a kind of nanoparticles with great potential value.

406 **2.6 FA-Dex-*b*-PPS-Dox induced apoptosis of PC3 cells through ROS production**

407 As research in nanotechnology for cancer treatment intensifies and its
408 applications broaden, the design of ROS-responsive nanodrug delivery system has
409 become an important platform for cancer diagnosis and therapy[49]. NADPH oxidase
410 4 (NOX4) is a member of the NADPH oxidase, which can catalyze the reduction of
411 molecular oxygen to various ROS[50]. The ROS produced by NOX4 are involved in
412 various biological functions such as cell apoptosis, differentiation and tumor
413 growth[51]. Dox, a kind of the most common cancer chemotherapeutic drugs, is
414 widely used in multiple clinical cancer therapy. It was reported that Dox can induce
415 the increase H₂O₂ levels, breaking the balance of oxidative stress in cells by
416 regulating the NOX4 expression levels[52]. These indicated that Dox could be used as
417 a potential drug to enhance H₂O₂ levels of cells. In this study, FA-Dex-*b*-PPS
418 nanocarriers were used to load traditional chemotherapy drug Dox to form a novel
419 nanomedicine (FA-Dex-*b*-PPS-Dox). On the one hand, Dox exerted traditional
420 chemotherapy effects. On the other hand, Dox increased the production of
421 intracellular H₂O₂ through NOX4 pathway, which further oxidized the PPS block,
422 thereby inducing a hydrophobic-hydrophilic transition, leading to the dissociation of
423 the polymer self-assembly and ultimately results in the rapid release of the drug. As
424 shown in Figure 6A and 6B, both Dex-*b*-PPS-Dox and FA-Dex-*b*-PPS-Dox could
425 increase the expression levels of NOX4. Further, flow cytometry (Figure 6C) and
426 CLSM (Figure 6D) were used to evaluate qualitatively and quantitatively the
427 production of intracellular ROS, respectively. FA-Dex-*b*-PPS-Dox significantly
428 increases intracellular ROS levels, demonstrating the targeted enhancement of
429 Dex-*b*-PPS-Dox with FA modification. In addition, glutathione (GSH) and superoxide
430 dismutase (SOD) levels reflect the antioxidant abilities of intracellular cells. As shown
431 in Figure 6E and 6F, compared with control group, Free Dox could increase both
432 intracellular GSH and SOD levels. FA-Dex-*b*-PPS-Dox significantly reduced GSH

433 and SOD levels, while there were no significant SOD levels differences after
434 Dex-*b*-PPS-Dox treatment. These results illustrated cell antioxidant status of different
435 treatments. Due to a series of intracellular redox chemical reactions after
436 FA-Dex-*b*-PPS-Dox treatment, all those reduced the antioxidant capacity of cancer
437 cells, resulting the reduction of GSH and SOD levels. In general, FA-Dex-*b*-PPS-Dox
438 elevated intracellular ROS levels, while depleted GSH and SOD levels.

439 Next, we further evaluated cell apoptosis using flow cytometry and western blot
440 assays, including the expression levels of Cleaved Caspase-3, a key factor of
441 apoptosis. The results, as shown in Figure 6G, 6H, and 6I, revealed that
442 FA-Dex-*b*-PPS-Dox treatment significantly induced apoptosis of PC3 cells when
443 compared with the control group. Additionally, the expression levels of Cleaved
444 Caspase-3 were significantly increased after Free Dox and FA-Dex-*b*-PPS-Dox
445 treatment, while Dex-*b*-PPS-Dox showed no significant difference. These findings
446 demonstrate that FA-Dex-*b*-PPS-Dox induces apoptosis of PC3 cells through ROS
447 production. Significantly, the findings of the present investigation imply that
448 FA-Dex-*b*-PPS-Dox may represent a potential therapeutic strategy for targeting PC3
449 tumor cells.

450 2.7 The antitumor efficacy of FA-Dex-*b*-PPS-Dox *in vivo*

451 To assess the efficacy of various treatments *in vivo*, male nude mice harboring
452 PC3 tumors were employed as the experimental animal model. The animal tumor
453 models were established by subcutaneously injecting 5×10^6 /mL PC3 cells. When the
454 tumor volume reached approximately 50-100 mm³, all mice were randomly divided
455 into 4 groups, namely Control, Free Dox, Dex-*b*-PPS-Dox, and FA-Dex-*b*-PPS-Dox,
456 and were injected through the tail vein with a dosage of 5 mg/kg Dox. Figure 7A and
457 7B display the tumor volume and weight after different treatments. The tumor volume
458 in mice treated with FA-Dex-*b*-PPS-Dox decreased notably compared to the control
459 groups, but there was no difference observed in the tumor volume of
460 FA-Dex-*b*-PPS-Dox compared with Dex-*b*-PPS-Dox. However, there was a
461 statistically significant difference between the tumor weight of FA-Dex-*b*-PPS-Dox

462 and Dex-*b*-PPS-Dox, indicating that FA-Dex-*b*-PPS-Dox effectively inhibited tumor
463 growth. This phenomenon could be explained by the specific absorption of
464 FA-Dex-*b*-PPS-Dox by the folic acid receptor on tumor cells.

465 The antitumor efficacy of FA-Dex-*b*-PPS-Dox was further validated through
466 hematoxylin-eosin and immunohistochemical staining of the tumor tissues, as
467 demonstrated in Figure 7C. Representative images showed a greater number of
468 obviously necrotic regions in tumor tissue after FA-Dex-*b*-PPS-Dox treatment using
469 hematoxylin-eosin staining. In addition, compared to the other groups, the ratio of
470 positive cells of Cleaved Caspase-3 was elevated, and the ratio of negative cells of
471 proliferating cell nuclear antigen (PCNA) was reduced after FA-Dex-*b*-PPS-Dox
472 treatment using immunohistochemistry staining. These findings indicate that
473 FA-Dex-*b*-PPS-Dox is capable of triggering apoptosis and inhibiting the proliferation
474 of cancer cells. Moreover, there were no significant changes in the body weight of the
475 four groups, as demonstrated in Figure 8A. Notably, the survival quality of mice after
476 Free Dox treatment was very poor, and the mortality rate of conventional
477 chemotherapy drugs Free Dox treatment was also high, with obvious hepatorenal
478 toxicity, as shown in Figure 8B and 8C.

479 To investigate the related toxicity of these nanomedicines *in vivo*, the major
480 metabolic organs, including the heart, liver, spleen, lung, and kidney, were evaluated
481 using hematoxylin-eosin staining. There was significant inflammatory cell infiltration
482 in the liver and kidney after Free Dox or Dex-*b*-PPS-Dox treatments, while
483 FA-Dex-*b*-PPS-Dox showed no obvious abnormalities in these major metabolic
484 organs. This indicates that the modification of FA could enhance the tumor targeting
485 of drugs and reduce accumulation in metabolic organs through the folic acid
486 receptor-mediated endocytosis process.

487 **3. Conclusion**

488 We report on the development of ROS-responsive Dex-*b*-PPS copolymers for
489 targeted oncotherapy. The Dex-*b*-PPS copolymers exhibit strong ROS responsiveness
490 and high loading capacity for Dox, and after modification with FA, they are capable

491 of targeted oncotherapy. Our studies have demonstrated that FA-Dex-*b*-PPS micelles
492 release Dox faster in response to 100 μ M H₂O₂. *In vitro* assays such as the CCK-8
493 assay, transwell assay, and wound healing assay, along with *in vivo* experiments on
494 xenograft mouse models, demonstrate that FA-Dex-*b*-PPS-Dox exhibits greater
495 antitumor effects compared to non-targeted Dex-*b*-PPS-Dox. These results suggest
496 that folic acid decorated Dex-*b*-PPS copolymers are a promising class of therapeutic
497 block copolymer nanoparticles that are ROS-responsive and have great potential in
498 the field of oncotherapy.

499 **4. EXPERIMENTAL SECTION**

500 *Materials:* 1-buthane thiol, 1,8-diazabicyclo [5.4.0] undec-7-ene (DBU) and
501 propylene sulfide (PS) (>96 %) were purchased from Tokyo Chemical Industry (TCI,
502 Japan). Propargyl bromide (99 %) was supplied by Alfa Aesar and used as received.
503 Dextran (Mn = 6600 g/mol) and Sodium azide (NaN₃, 99 %) were obtained from
504 Sigma-Aldrich. Sodium cyanoborohydride (NaBH₃CN, 98 %) and
505 3-chloropropylamine hydrochloride (98 %) were acquired from Aladdin Chemical
506 Company (Shanghai, China). Copper sulfate pentahydrate (CuSO₄•5H₂O, 99 %) and
507 sodium ascorbate (NaAsc, 99 %) were acquired from Macklin Chemical Company
508 (Shanghai, China). Doxorubicin hydrochloride (Dox•HCl) was purchased from
509 Meilunbio (Dalian, China). Tetrahydrofuran (THF, chromatographic grade, >99.9 %)
510 and dichloromethane (DCM, Chromatographic grade, >99.9 %) were obtained from
511 J&K Chemical Reagent Inc (Beijing, China) and used as received without further
512 purification. All additional chemicals were utilized in their as-received state without
513 undergoing any additional purification steps.

514 *Methods—Bioinformatics analysis:* The Cancer Genome Atlas (TCGA)
515 pan-cancer dataset, which encompasses RNA-sequencing data and curated clinical
516 phenotypes for 34 prevalent cancer types, was obtained from the Pan-Cancer Atlas
517 Hub within the University of California Santa Cruz (UCSC) Xena dataset
518 (<https://xenabrowser.net/>). Specifically, transcriptome data for the FOLH1 gene were
519 extracted from 34 tumor types, including glioblastoma (GBM, t=153, n=1157),

520 glioblastoma multiforme (GBMLGG, t=662, n=1157), lower grade glioma (LGG,
521 t=509, n=1157), uterine corpus endometrioid carcinoma (UCEC, t=180, n=23), breast
522 invasive carcinoma (BRCA, t=1092, n=292), cervical squamous cell carcinoma and
523 endocervical adenocarcinoma (CESC, t=304, n=13), lung adenocarcinoma (LUAD,
524 t=513, n=397), esophageal squamous cell carcinoma (ESCA, t=181, n=668), stomach
525 and intestinal stromal tumor (STES, t=595, n=879), kidney renal papillary cell
526 carcinoma (KIRP, t=288, n=168), kidney and pancreas cancer (KIPAN, t=884, n=168),
527 colorectal adenocarcinoma (COAD, t=288, n=349), colorectal and rectal
528 adenocarcinoma (COADREAD, t=380, n=159), prostate adenocarcinoma (PRAD,
529 t=495, n=152), stomach adenocarcinoma (STAD, t=414, n=211), head and neck
530 squamous cell carcinoma (HNSC, t=518, n=44), kidney renal clear cell carcinoma
531 (KIRC, t=530, n=168), lung squamous cell carcinoma (LUSC, t=498, n=397), liver
532 hepatocellular carcinoma (LIHC, t=369, n=160), Wilms tumor (WT, t=120, n=168),
533 skin cutaneous melanoma (SKCM, t=102, n=558), bladder urothelial carcinoma
534 (BLCA, t=407, n=28), thyroid carcinoma (THCA, t=504, n=338), rectal
535 adenocarcinoma (READ, t=92, n=10), ovarian serous cystadenocarcinoma (OV, t=419,
536 n=88), pancreatic adenocarcinoma (PAAD, t=178, n=171), testicular germ cell tumor
537 (TGCT, t=148, n=165), uterine corpus sarcoma (UCS, t=57, n=78), acute
538 lymphoblastic leukemia (ALL, t=132, n=337), acute myeloid leukemia (LAML,
539 t=173, n=337), pheochromocytoma and paraganglioma (PCPG, t=177, n=3),
540 adenocarcinoma of the breast (ACC, t=77, n=128), kidney chromophobe (KICH, t=66,
541 n=168), cholangiocarcinoma (CHOL, t=36, n=9), as well as relevant paracancerous
542 tissues.

543 The dataset for this study was sourced from the Uniform Standardized Pan-Cancer
544 dataset provided by the University of California, Santa Cruz (UCSC) database
545 (<https://xenabrowser.net/>) – the TCGA Pan-Cancer (PANCAN), which encompasses
546 10,535 samples and 60,499 genes. Building upon this foundation, we extracted the
547 expression data for the ENSG00000086205 (FOLH1) gene across various samples.
548 Subsequently, we further refined our selection to include samples derived from

549 primary blood-derived cancers (Peripheral Blood) and primary tumors. Following the
550 methodology outlined in the previous study (Malta, T. M. et al, 2018), we computed
551 the RNAss tumor stemness scores corresponding to the mRNA characteristics of each
552 tumor. Thereafter, we integrated the stemness indices with gene expression data and
553 applied a $\log_2(x+1)$ transformation to each expression value. After excluding cancer
554 types with fewer than three samples, we ultimately obtained expression data for 37
555 cancer types.

556 *Methods—Methods and Instrumentation:* The infrared absorption spectra of the
557 samples were measured using a Perkin-Elmer Paragon 1000 infrared spectrometer,
558 USA. The chemical structure of the polymers was analyzed using a Bruker NMR
559 instrument (Bruker AV-500). All deuterated solvents were purchased from Sigma and
560 tetramethylsilane (TMS) was used as an internal standard. Particle size and particle
561 distribution index (PDI) were determined by using a Malvern particle sizer (Malvern
562 Nano-ZS/ZEN-3600 Zetasizer). The dry-state morphology of the nanoparticles was
563 examined utilizing a transmission electron microscope (TEM, JEM-2100F, JEOL,
564 Tokyo, Japan). A minute quantity of the nanoparticle suspension was deposited onto a
565 copper grid, and following a one-minute interval, the excess solution was
566 meticulously blotted away using filter paper. Subsequently, the specimens were
567 subjected to negative staining with a 1 wt% phosphotungstic acid solution. A small
568 phosphotungstic acid solution droplet was cover the sample, after 20 seconds the
569 excess phosphotungstic acid solution was carefully blotted off with filter paper. Prior
570 to TEM observation, samples are stored in a desiccator to remove excess moisture.
571 The critical micelle concentration (cmc) for the block copolymer was ascertained
572 through the application of the widely employed pyrene fluorescence probe technique.
573 Briefly, 50 μL of acetone solution containing pyrene 6×10^{-5} mol/L was added to a 10
574 mL EP tube, and the acetone was removed via evaporation. Various concentrations of
575 the block polymer's aqueous solutions were introduced into EP tubes, which were
576 subsequently agitated in the absence of light for 24 h at 37 °C on a
577 temperature-controlled shaker before conducting the tests. The tests were carried out

578 using a Shimadzu RF-5301PC fluorescence spectrophotometer. The excitation
579 spectrum was scanned in the wavelength range of 300-350 nm, with an emission
580 wavelength of 373 nm and a slit width of 5 nm. The fluorescence spectra of pyrene in
581 the nanoparticle solution were recorded separately under two different conditions, that
582 is, PBS (50 mM, pH 7.4) without any H₂O₂ or PBS (50 mM, pH 6.5) with 100 μM
583 H₂O₂. The intensity ratio of fluorescence intensity at 337 nm and 335 nm was used as
584 the vertical coordinate and the logarithm of micelle concentration was used as the
585 horizontal coordinate. The concentration value corresponding to the intersection of
586 the data points is the measured cmc. The concentration of Dox in the aqueous solution
587 was measured using a Shimadzu UV-3150 UV-Vis spectrometer and the absorbance
588 intensity at 480 nm was recorded. A working curve was established by measuring the
589 UV absorption at 480 nm for a series of known concentrations of aqueous Dox
590 solutions.

591 *Methods—Preparation of α -alkyne Poly(Propylene sulfide) (alkyne-PPS):*
592 α -alkyne poly(propylene sulfide) can be synthesized via a combination of anionic
593 polymerization of propylene sulfide and termination with propargyl bromide. Prior to
594 anionic polymerization, the monomer propylene sulfide is first purified by distillation.
595 The anionic polymerization process of propylene sulfide is based on the method
596 previously reported in the literature[23]. A 100 mL flame-dried round-bottom flask
597 was filled with DBU (4 mmol, 0.60 mL) and 20 mL of ultra-dry THF, and then
598 degassed with argon gas for 30 minutes. The flask was placed in a cold trap to keep
599 the solution temperature below 0 °C. The pre-degassed THF solution containing
600 1-buthane thiol (1.0 mmol, 0.07 mL) was then slowly dripped into the flask via a
601 dropping funnel, and the reaction was continued for 30 minutes to activate the initiator.
602 The degassed propylene sulfide (80 mmol, 6.24 mL) monomer was then added to the
603 round-bottom flask in one go using a syringe, and the reaction was stirred for 2 h at a
604 temperature of no more than 0 °C. Propargyl bromide (2 mmol, 0.24 g) was added to
605 the reaction system to terminate the anionic polymerization reaction and to introduce
606 an alkyne group. After 12 h of reaction, the resulting salt was removed by filtration,

607 and most of the THF was distilled out under reduced pressure. The mixture was then
608 dropped into cold anhydrous ether to give a white precipitate, which was collected,
609 washed three times with ether, and dried under vacuum to yield a white viscous
610 polymer. ¹H NMR (500 MHz; CDCl₃, δ): 0.9-0.95 (t, CH₃CH₂), 1.35-1.41 (s, CH₃CH),
611 1.45-1.52 (s, -CH₂CH₂CH₂), 1.53-1.60 (m, CH₃CH₂CH₂), 2.50-2.56 (t, CH≡C-),
612 2.56-2.70 (s, CHCH₂S), 2.83-2.98 (t, SCHCH₂).

613 *Methods—Preparation of α-azide Dextran (azide-Dex):* The azide functionality
614 was incorporated into the reducing end of dextran by employing a previously
615 documented procedure, albeit with slight modifications [53]. Initially, a mixture
616 consisting of 2 g of dextran and 40 mL of deionized water was prepared in a 100 mL
617 round-bottomed flask. After complete dissolution of the dextran, 15 g of
618 3-chloropropylamine hydrochloride and 2 g of NaBH₃CN were added to the flask.
619 The reaction vessel was secured with a rubber stopper throughout the process. The
620 reaction solution was agitated in an oil bath maintained at 50 °C for a duration of 7
621 days, during which time 3 g of NaBH₃CN was added daily. Upon completion of the
622 reaction, the product was decanted into a dialysis membrane (1000 Da) and subjected
623 to dialysis against deionized water for a period of three days to remove residual
624 inorganic contaminants. It should be highlighted that throughout the dialysis
625 procedure, the volume of the mixed solution in the dialysis tube increases
626 significantly, and the collected dialysate must be concentrated before the next reaction.
627 The aqueous fraction of the mixture was largely evaporated through vacuum
628 distillation, resulting in a volume of approximately 30 mL of solution. Subsequently, 2
629 g of sodium azide were introduced into the solution, followed by stirring in an oil bath
630 heated to 80 °C for a duration of 24 h. The product was then subjected to dialysis
631 against deionized water over a three-day period to eliminate surplus inorganic salts.
632 The process was concluded with the acquisition of a white powder, achieved by
633 lyophilizing the dialysate.

634 *Methods—Synthesis of dextran-block-poly(propylene sulfide) copolymer by*
635 *Husigen Cycloaddition:* Copper(I)-catalyzed azide/alkyne Husigen cycloaddition has

636 been widely utilized to prepare block polymers that incorporate polysaccharide chain
637 segments[35]. In this work, a polysaccharide-based diblock copolymer was
638 synthesized via the Huisgen cycloaddition between alkyne-PPS and azide-Dex. In a
639 representative procedure, 0.16 g of azide-modified dextran was transferred into a 50
640 mL round-bottomed flask, which already held 25 mL of DMSO. Viscous PPS is hard
641 to dissolve directly in DMSO, so 0.1 g of alkyne-PPS was dissolved in 4 mL of THF
642 and then slowly added dropwise to the DMSO solution. To prevent the oxidation of
643 cuprous ions by oxygen dissolved in the DMSO, a high-purity argon gas was
644 continuously passed through the DMSO to remove oxygen. $\text{CuSO}_4 \cdot 5\text{H}_2\text{O}$ and NaAsc
645 were subsequently added, and the flask was further maintained under an argon
646 atmosphere for 10 minutes. The flask was sealed with a rubber stopper, and the
647 mixture was stirred in an oil bath at 50 °C for 3 days. After the reaction, the mixture
648 was transferred to dialysis tubes (50 kDa) and dialyzed with deionized water
649 containing 0.01 % EDTA-Na for 2 days, followed by dialysis with deionized water for
650 another 2 days to remove excess inorganic salts and azide-Dex. The dialysate was
651 lyophilized to obtain white powder.

652 *Methods—Preparation of folic acid decorated dextran-block-poly(propylene*
653 *sulfide) (FA-Dex-b-PSS) copolymer via esterification reaction:* The hydroxyl groups
654 present on dextran provides an opportunity for esterification with the carboxyl group
655 of folic acid. In this study, folic acid decorated Dex-*b*-PSS was synthesized following
656 a previously reported procedure[54]. Briefly, 0.02 g of FA was dissolved in 15 mL of
657 anhydrous DMSO. After the folic acid had fully dissolved, to the flask, 0.1 g of
658 Dex-*b*-PSS was introduced, after which EDCI (0.017 g, 0.09 mmol) and HOBT
659 (0.012 g, 0.09 mmol) were sequentially added. Subsequently, the flask was sealed,
660 wrapped in aluminum foil, and agitated at ambient temperature for a period of two
661 days. After the reaction was complete, the reaction mixture was packed into dialysis
662 bags (6 kDa) and dialyzed for three days to remove excess folic acid and DMSO. The
663 dialysate was lyophilized, yielding a yellow powder. The degree of substitution of
664 folic acid can be calculated using methods previously described in literature[54].

665 *Methods— ROS sensitive-nanoparticles preparation and characterization:* The
666 FA-Dex-*b*-PSS amphiphilic copolymer is capable of undergoing self-assembly to
667 produce nanoparticles in chosen solvents. Then, 10 mg of FA-Dex-*b*-PSS was
668 dissolved in 1.5 mL of warm DMSO under continuous stirring. The combined
669 solution was incrementally introduced into 5 mL of deionized water under continuous
670 stirring for 1 h. Subsequently, the mixture was transferred to a dialysis sack with a 6
671 kDa molecular weight cutoff and subjected to dialysis against deionized water for a
672 duration of 2 days to eliminate the organic solvents. Following this, the dialysate was
673 filtered through a 0.22 µm pore-size syringe filter. The dimensions and dispersal of
674 the synthesized nanoparticles were assessed utilizing a Malvern particle size analyzer.
675 The dried state morphology of the nanoparticles was examined with a JEOL
676 JEM-2100F transmission electron microscope. The critical micelle concentration of
677 the block polymer was ascertained using the established pyrene fluorescence probe
678 technique, employing a Shimadzu RF-5301PC fluorescence spectrophotometer.

679 *Methods— Dox loaded and in vitro release:* To incorporate Dox within the
680 internal compartment of the nanoparticles, a solution containing 10 mg of
681 FA-Dex-*b*-PSS and 1 mg of Dox•HCl was prepared by dissolving them in warm
682 DMSO. Triethylamine was added in an equivalent amount to neutralize the
683 hydrochloride, and the resulting mixture was dropped into deionized water with
684 continuous stirring. Following this, the solution was decanted into a dialysis tube and
685 subjected to dialysis against deionized water for a period of 24 h. The resulting
686 dialysate was then passed through a needle filter. The concentration of Dox was
687 determined using an established standard curve, and the drug loading content (DLC)
688 was calculated using the following formula:

$$689 \quad \text{DLC(\%)} = w_1/w_2 \times 100 \quad (1)$$

690 where w_1 is the weight of Dox loaded in the nanoparticles and w_2 represents the
691 weight of FA-Dex-*b*-PSS.

692 *In vitro* drug release was conducted under various conditions, including pH 7.4
693 without H₂O₂, pH 6.5 without H₂O₂, pH 4.5 without H₂O₂, pH 7.4 with 500 µM H₂O₂,

694 pH 7.4 with 100 μ M H₂O₂, and pH 6.5 with 100 μ M H₂O₂. To begin, 3 mL of
695 drug-loaded nanoparticle solution was placed into a dialysis bag and transferred to a
696 centrifuge tube containing 27 mL of PBS at different pH and H₂O₂ concentrations.
697 The tubes were then sealed and placed into a 37 °C water bath, where they were
698 agitated at 100 rpm. At predetermined time intervals, 3 mL of solution outside the
699 dialysis bag was withdrawn and replaced with 3 mL of fresh buffer solution. The drug
700 release experiment was repeated three times, and the Dox concentration was measured
701 at 480 nm using a UV-Vis spectrometer (UV-3150, Shimadzu, Japan). The
702 accumulated percentage of released Dox was calculated using the following equation:

$$703 \quad E_r(\%) = \frac{V_e \sum_{i=1}^{n-1} C_i + V_0 C_n}{m_{\text{DOX}}} \times 100\% \quad (2)$$

704 In which m_{DOX} denotes the mass of doxorubicin within the micelles, V_0 signifies
705 the total volume of the release medium (V_0 is 30 mL), V_e is the volume of the medium
706 exchanged ($V_e = 3$ mL), and C_i is the concentration of DOX in the i th aliquot.

707 *Methods—CCK-8 assay:* Human prostate cancer cell lines PC3 was maintained in
708 RPMI-1640 medium (Hyclone, United States) that contained 10 % fetal bovine serum
709 (FBS) and 1 % penicillin-streptomycin, within a 37°C incubator under a 5% CO₂
710 environment. CCK-8 assay was conducted to evaluate the in vitro biocompatibility of
711 FA-Dex-*b*-PPS and the inhibition of cell proliferation of Free Dox, Dex-*b*-PPS-Dox,
712 and FA-Dex-*b*-PPS-Dox to PC3 cells. Briefly, cells were plated into 96-well plates at
713 a density of approximately 1×10^4 cells/well. After 24 h or 48 h incubation with
714 different treatments, 10 μ L solution of different treatments concentrations were added
715 to the appropriate wells for appropriate time in a 5 % CO₂ incubator at 37 °C.
716 Subsequently, 10 μ L of the CCK-8 reagent were added to each well, and the plate was
717 further incubated for a period of 2 to 4 h. The optical density of each well was then
718 quantified at a wavelength of 450 nm using a multimode plate reader.

719 *Methods—Transwell assay:* The upper surface of the lower membrane in the
720 transwell chamber was coated with a solution of Matrigel at a concentration of 50
721 mg/L, diluted 1:8. The cells were incubated in serum-free RPMI 1640 medium for a
722 duration of 12 h, and the 5×10^5 PC3 cells density of cell suspension was adjusted. A

723 200 μ L volume of cell suspension was introduced into the upper compartment of the
724 transwell insert, while 600 μ L of medium supplemented with 10% FBS was placed in
725 the lower chamber of the 24-well culture plate. The 24 well culture plates were placed
726 in 5 % CO₂ incubator at 37 °C for 24 h. Afterward, the cells in the upper layer of the
727 cell membrane were wiped with a cotton swab, and the rest of cells were fixed with
728 4 % paraformaldehyde for 20 minutes and dyed with crystal violet solution for 15
729 minutes. After the chambers were dried, pictures were taken under the microscope and
730 conducted comparative analysis. Each sample is randomly counted for 10 visual fields,
731 and the average value is taken.

732 *Methods—Wound healing assay:* PC3 cells were plated and grown to 90%
733 confluence in a six-well plate overnight. Following this, wounds were created using a
734 200- μ L sterile pipette tip, and any cellular debris was subsequently cleared away. The
735 cells were incubated in the medium solution of different treatments: Control (PBS),
736 Free Dox, Dex-*b*-PPS-Dox, and FA-Dex-*b*-PPS-Dox. The images of distance
737 migrated by the cells were taken at 0 and 24 h after wound scratching through a
738 microscope (Leica, Germany) in the same position of the plate. The experiments were
739 conducted in triplicate independently.

740 *Methods—Cellular uptake:* PC3 cells were treated with PBS, Free Dox,
741 Dex-*b*-PPS-Dox, and FA-Dex-*b*-PPS-Dox maintaining Dox content 5 μ g/mL for 8 h
742 with Hoechst for 10 min after washing with PBS. Then cellular uptake of different
743 group by confocal laser scanning microscope.

744 *Methods—Reactive oxygen species generation:* The intracellular levels of ROS
745 were quantified using a dedicated ROS assay kit (beyotime, China). The attached PC3
746 cells were treated with different treatments (Control, Free Dox, Dex-*b*-PPS-Dox, and
747 FA-Dex-*b*-PPS-Dox) for 8 h. After the incubation, harvested cells were treated with 1
748 μ L DHE (S0033, Beyotime Biotechnology, Shanghai, China) at 37 °C with CO₂ in the
749 dark for 30 minutes. Subsequently, the cells underwent two PBS washes and were
750 then disaggregated into a uniform single-cell suspension. The fluorescent intensity
751 was analyzed by flow cytometry (BD Bioscience).

752 *Methods— Apoptosis assay:* The Annexin-V apoptosis detection kit was utilized
753 to assess the apoptotic status of PC3 cells that had been subjected to Control (PBS),
754 Free Dox, Dex-*b*-PPS-Dox, and FA-Dex-*b*-PPS-Dox. PC3 cells were seeded and
755 incubated for 24 h to reach 80 % confluency in a six-well plate. Then, the cells were
756 treated with different treatments for 24 h at 37 °C in a CO₂ incubator. Subsequently,
757 the cells were harvested and rinsed with chilled PBS, and then redispersed in 1×
758 binding buffer at a concentration of 1×10⁶ cells per milliliter. The cell suspension was
759 then incubated with Annexin-V at ambient temperature in a light-shielded setting.
760 Whereafter, before being analyzed by flow cytometry, the cells were washed,
761 re-suspended, and PI was added. Using the FACS Calibur flow cytometer, the
762 fluorescence intensity was analyzed and repeated three times. All analysis was carried
763 out using FlowJo software.

764 *Methods— Western blot analysis:* PC3 cells subjected to various treatments
765 underwent two PBS washes and were subsequently lysed using an ice-cold
766 Radio-Immunoprecipitation Assay (RIPA) buffer containing 1mM PMSF, from which
767 total protein extracts were obtained. The concentration of total protein was quantified
768 using the BCA protein assay kit. Separation of proteins was achieved through
769 electrophoretic techniques utilizing 10% SDS-polyacrylamide gel matrices, followed
770 by the complete transfer of the desired protein fractions onto polyvinylidene
771 difluoride membranes. Subsequent to this, the membranes were subjected to a
772 blocking step using 5% non-fat dry milk in TBST buffer at ambient temperature for a
773 duration of 1 h. This was followed by an overnight incubation at 4°C with specific
774 primary antibodies against NOX4, Cleaved Caspase-3, and β-actin. After thorough
775 washing with TBST buffer on three separate occasions, the membranes were then
776 probed with horseradish peroxidase-conjugated secondary antibodies for an hour at
777 37°C. β-actin served as the internal reference for normalization purposes. All
778 experiments were carried out with three replicates. Blots were determined using
779 chemiluminescence detection system membranes. Image J software (version 1.8.0,
780 NIH, USA) was used to quantify the intensity of the immunoreactive bands.

781 *Methods— In vivo antitumor study:* Animal studies were conducted with BALB/c
782 mice aged between 4 to 6 weeks. All experiments were handled based on the relevant
783 principles of the Guide for the Care and Use of Laboratory Animals and approved by
784 the ethics committee of the South China University of Technology (Approval no.
785 S-2023-078-01). Experimental animals were allocated to various groups in a random
786 fashion. For tumor induction, approximately 5×10^6 PC3 cells were harvested and
787 administered subcutaneously to the right flanks of nude mice, and tumor growth was
788 monitored until the volume reached 50-100 mm³. The test animals received a single
789 intravenous dose of the therapeutic agent at 5 mg/kg body weight, administered every
790 other day for a total of five injections. In contrast, the control group received an
791 equivalent volume of PBS via the same route. Tumor dimensions and the body weight
792 of the mice were recorded throughout the study. Following the completion of the
793 treatment regimen, mice were euthanized via cervical dislocation. Subsequent to
794 euthanasia, hematoxylin and eosin (H&E) staining was utilized to examine the
795 histological features of tumor tissues as well as the primary organs, including the
796 heart, liver, spleen, lungs, and kidneys.

797

798 **Acknowledgements**

799 Y.Z., Z.L., Z.H., and J.L. contributed equally to this work. We acknowledge the
800 technical support provided by Biorender for the creation of the schematic diagrams
801 presented in this manuscript. This study was funded by The Guangdong Basic and
802 Applied Basic Research Foundation (2021A1515220060, 2022A1515110245,
803 2023A1515012320), The Guangdong Natural Science Foundation
804 (2024A1515012177), the National Natural Science Foundation of China (81971574,
805 82271938, 82272276, 82373166), The Science and Technology Development Fund,
806 Macau SAR (0031/2021/A, 0090/2022/A), the Science and Technology Project of
807 Guangzhou (2023A03J0969), and the special fund for the construction of high-level
808 key clinical specialty (medical imaging) in Guangzhou, and Guangzhou key
809 laboratory of molecular imaging and clinical translational medicine (202201020376).

810

811 **Conflict of Interest**

812 The authors report no conflict of interest in the present study.

813

814 **Declaration of competing interest**

815 The authors declare that they have no known competing financial interests or
816 personal relationships that could have appeared to influence the work reported in this
817 paper.

818

819 **Data availability Statement**

820 All the data associated with this study are presented in the paper or in the
821 Supporting Information.

822

823 **Keywords**

824 Folic acid, Copolymer nanoparticles, Prostate cancer.

825

826 **References**

- 827 1. Siegel, R. L.; Miller, K. D.; Fuchs, H. E.; Jemal, A., *CA: a cancer journal for clinicians* **2022**, *72*(1),
828 7-33. DOI 10.3322/caac.21708.
- 829 2. Yu, L.; Sui, B.; Fan, W.; Lei, L.; Zhou, L.; Yang, L.; Diao, Y.; Zhang, Y.; Li, Z.; Liu, J.; Hao, X.,
830 *Journal of extracellular vesicles* **2021**, *10*(3), e12056. DOI 10.1002/jev2.12056.
- 831 3. Sridaran, D.; Bradshaw, E.; DeSelm, C.; Pachynski, R.; Mahajan, K.; Mahajan, N. P., *Cell reports*.
832 *Medicine* **2023**, *4*(10), 101199. DOI 10.1016/j.xcrm.2023.101199.
- 833 4. Allen, T. M.; Cullis, P. R., *Science (New York, N.Y.)* **2004**, *303*(5665), 1818-22. DOI
834 10.1126/science.1095833.
- 835 5. Sharifi-Azad, M.; Fathi, M.; Cho, W. C.; Barzegari, A.; Dadashi, H.; Dadashpour, M.;
836 Jahanban-Esfahlan, R., *Cancer cell international* **2022**, *22*(1), 196. DOI
837 10.1186/s12935-022-02605-y.
- 838 6. Lee, J.; Kim, K.; Kwon, I. C.; Lee, K. Y., *Advanced materials (Deerfield Beach, Fla.)* **2023**, *35*(10),
839 e2207342. DOI 10.1002/adma.202207342.
- 840 7. Liu, P.; Wu, Y.; Xu, X.; Fan, X.; Sun, C.; Chen, X.; Xia, J.; Bai, S.; Qu, L.; Lu, H.; Wu, J.; Chen, J.;
841 Piao, J.-G.; Wu, Z., *Nano Research* **2023**, *16*(7), 9688-9700. DOI 10.1007/s12274-023-5541-1.
- 842 8. Donadoni, E.; Siani, P.; Frigerio, G.; Di Valentin, C., *Nanoscale* **2022**, *14*(33), 12099-12116.

843 DOI 10.1039/d2nr02603a.

844 9. Dominguez-Martinez, I.; Joaquin-Ovalle, F.; Ferrer-Acosta, Y.; Griebenow, K. H.,
845 *Pharmaceutics* **2022**, *14* (3). DOI 10.3390/pharmaceutics14030490.

846 10. Zhu, J.; Li, H.; Xiong, Z.; Shen, M.; Conti, P. S.; Shi, X.; Chen, K., *ACS applied materials &*
847 *interfaces* **2018**, *10* (41), 34954-34964. DOI 10.1021/acsami.8b12355.

848 11. Du, W.; Lu, Q.; Zhang, M.; Cao, H.; Zhang, S., *ACS applied bio materials* **2021**, *4* (4),
849 3246-3255. DOI 10.1021/acsabm.0c01612.

850 12. DeCarlo, A.; Malardier-Jugroot, C.; Szewczuk, M. R., *Bioconjugate chemistry* **2021**, *32* (3),
851 512-522. DOI 10.1021/acs.bioconjchem.0c00625.

852 13. Shams, A.; Shabani, R.; Asgari, H.; Karimi, M.; Najafi, M.; Asghari-Jafarabadi, M.; Razavi, S. M.;
853 Miri, S. R.; Abbasi, M.; Mohammadi, A.; Koruji, M., *Nanomedicine (London, England)* **2022**, *17* (8),
854 531-545. DOI 10.2217/nnm-2021-0210.

855 14. Omurtag Ozgen, P. S.; Atasoy, S.; Zengin Kurt, B.; Durmus, Z.; Yigit, G.; Dag, A., *Journal of*
856 *materials chemistry. B* **2020**, *8* (15), 3123-3137. DOI 10.1039/c9tb02711d.

857 15. Wang, X.; Li, C.; Wang, Y.; Chen, H.; Zhang, X.; Luo, C.; Zhou, W.; Li, L.; Teng, L.; Yu, H.; Wang,
858 J., *Acta pharmaceutica Sinica. B* **2022**, *12* (11), 4098-4121. DOI 10.1016/j.apsb.2022.08.013.

859 16. Lin, J. T.; Du, J. K.; Yang, Y. Q.; Li, L.; Zhang, D. W.; Liang, C. L.; Wang, J.; Mei, J.; Wang, G. H.,
860 *Materials science & engineering. C, Materials for biological applications* **2017**, *81*, 478-484. DOI
861 10.1016/j.msec.2017.08.036.

862 17. Ding, H.; Tan, P.; Fu, S.; Tian, X.; Zhang, H.; Ma, X.; Gu, Z.; Luo, K., *Journal of controlled*
863 *release : official journal of the Controlled Release Society* **2022**, *348*, 206-238. DOI
864 10.1016/j.jconrel.2022.05.056.

865 18. Ge, C.; Zhu, J.; Wu, G.; Ye, H.; Lu, H.; Yin, L., *Biomacromolecules* **2022**, *23* (6), 2647-2654. DOI
866 10.1021/acs.biomac.2c00399.

867 19. Zhang, Y.; Li, Y.; Huang, S.; Zhang, H.; Lin, Q.; Gong, T.; Sun, X.; Zhang, Z.; Zhang, L.,
868 *Nanoscale* **2021**, *13* (36), 15267-15277. DOI 10.1039/d1nr02964a.

869 20. Su, M.; Xiao, S.; Shu, M.; Lu, Y.; Zeng, Q.; Xie, J.; Jiang, Z.; Liu, J., *Colloids and surfaces. B,*
870 *Biointerfaces* **2020**, *193*, 111067. DOI 10.1016/j.colsurfb.2020.111067.

871 21. Lee, S. H.; Gupta, M. K.; Bang, J. B.; Bae, H.; Sung, H. J., *Adv Healthc Mater* **2013**, *2* (6), 908-15.
872 DOI 10.1002/adhm.201200423.

873 22. Ye, H.; Zhou, Y.; Liu, X.; Chen, Y.; Duan, S.; Zhu, R.; Liu, Y.; Yin, L., *Biomacromolecules* **2019**, *20*
874 (7), 2441-2463. DOI 10.1021/acs.biomac.9b00628.

875 23. Gupta, M. K.; Martin, J. R.; Werfel, T. A.; Shen, T.; Page, J. M.; Duvall, C. L., *Journal of the*
876 *American Chemical Society* **2014**, *136* (42), 14896-902. DOI 10.1021/ja507626y.

877 24. Cerritelli, S.; O'Neil, C. P.; Velluto, D.; Fontana, A.; Adrian, M.; Dubochet, J.; Hubbell, J. A.,
878 *Langmuir : the ACS journal of surfaces and colloids* **2009**, *25* (19), 11328-35. DOI
879 10.1021/la900649m.

880 25. Allen, S. D.; Liu, Y. G.; Kim, T.; Bobbala, S.; Yi, S.; Zhang, X.; Choi, J.; Scott, E. A., *Biomaterials*
881 *science* **2019**, *7* (2), 657-668. DOI 10.1039/c8bm01224e.

882 26. Velluto, D.; Demurtas, D.; Hubbell, J. A., *Molecular pharmaceutics* **2008**, *5* (4), 632-42. DOI
883 10.1021/mp7001297.

884 27. Wu, W.; Chen, M.; Luo, T.; Fan, Y.; Zhang, J.; Zhang, Y.; Zhang, Q.; Sapin-Minet, A.; Gaucher,
885 C.; Xia, X., *Acta biomaterialia* **2020**, *103*, 259-271. DOI 10.1016/j.actbio.2019.12.016.

886 28. Zeng, Z.; Chen, S.; Chen, Y., *ChemMedChem* **2023**, *18* (20), e202300245. DOI

887 10.1002/cmdc.202300245.

888 29. Napoli, A.; Tirelli, N.; Kilcher, G.; Hubbell, J. A., *Macromolecules* **2001**, *34*, 8913-8917.

889 30. McSweeney, M. D.; Wessler, T.; Price, L. S. L.; Ciociola, E. C.; Herity, L. B.; Piscitelli, J. A.;
890 Zamboni, W. C.; Forest, M. G.; Cao, Y.; Lai, S. K., *Journal of controlled release : official journal of*
891 *the Controlled Release Society* **2018**, *284*, 171-178. DOI 10.1016/j.jconrel.2018.06.002.

892 31. Hong, L.; Wang, Z.; Wei, X.; Shi, J.; Li, C., *Journal of pharmacological and toxicological*
893 *methods* **2020**, *102*, 106678. DOI 10.1016/j.vascn.2020.106678.

894 32. Yazdi, M. K.; Sajadi, S. M.; Seidi, F.; Rabiee, N.; Fatahi, Y.; Rabiee, M.; Dominic, C. D. M.;
895 Zarrintaj, P.; Formela, K.; Saeb, M. R.; Bencherif, S. A., *Progress in polymer science* **2022**, *133*. DOI
896 10.1016/j.progpolymsci.2022.101590.

897 33. Song, S. G.; Oh, C.; Yoo, S.; Cho, J. Y.; Kim, K. S.; Song, C.; Premkumar, T., *International journal*
898 *of biological macromolecules* **2023**, *253* (Pt 5), 127069. DOI 10.1016/j.ijbiomac.2023.127069.

899 34. Yang, H.; Zhang, L. M., *International journal of biological macromolecules* **2021**, *181*,
900 1243-1253. DOI 10.1016/j.ijbiomac.2021.05.101.

901 35. Schatz, C.; Louguet, S.; Le Meins, J. F.; Lecommandoux, S., *Angewandte Chemie*
902 *(International ed. in English)* **2009**, *48* (14), 2572-5. DOI 10.1002/anie.200805895.

903 36. Soleymani, M.; Poorkhani, A.; Khalighfard, S.; Velashjerdi, M.; Khori, V.; Khodayari, S.;
904 Khodayari, H.; Dehghan, M.; Alborzi, N.; Agah, S.; Alizadeh, A. M., *Scientific reports* **2023**, *13* (1),
905 13560. DOI 10.1038/s41598-023-40627-2.

906 37. Ngo, L.; Knothe Tate, M. L., *Scientific reports* **2023**, *13* (1), 9119. DOI
907 10.1038/s41598-023-30322-7.

908 38. Tian, H.; Yu, L.; Zhang, M.; He, J.; Sun, X.; Ni, P., *Colloids and surfaces. B, Biointerfaces* **2023**,
909 *228*, 113400. DOI 10.1016/j.colsurfb.2023.113400.

910 39. Schatz, C.; Lecommandoux, S., *Macromolecular rapid communications* **2010**, *31* (19),
911 1664-84. DOI 10.1002/marc.201000267.

912 40. Yue, Y.; Li, H.; Wang, X.; Zhang, B.; Li, Y.; Liu, Y.; Ma, X.; Liu, G.; Zhao, X.; Shi, J., *ACS applied*
913 *materials & interfaces* **2023**, *15* (37), 44175-44185. DOI 10.1021/acsami.3c06674.

914 41. Yang, X.; Chen, Y.; Yuan, R.; Chen, G.; Blanco, E.; Gao, J.; Shuai, X., *Polymer* **2008**, *49* (16),
915 3477-3485. DOI <https://doi.org/10.1016/j.polymer.2008.06.005>.

916 42. Reed, G. A., *Current protocols in pharmacology* **2016**, *75*, 7.6.1-7.6.12. DOI
917 10.1002/cpph.16.

918 43. Wilhelm, M.; Zhao, C. L.; Wang, Y.; Xu, R.; Winnik, M. A.; Mura, J. L.; Riess, G.; Croucher, M. D.,
919 *Macromolecules* **1991**, *24* (5), 1033-1040. DOI 10.1021/ma00005a010.

920 44. Chang, L.; Deng, L.; Wang, W.; Lv, Z.; Hu, F.; Dong, A.; Zhang, J., *Biomacromolecules* **2012**, *13*
921 (10), 3301-10. DOI 10.1021/bm301086c.

922 45. Choi, K. H.; Nam, K. C.; Cho, G.; Jung, J. S.; Park, B. J., *Nanomaterials (Basel, Switzerland)* **2018**,
923 *8* (9). DOI 10.3390/nano8090722.

924 46. Au, K. M.; Satterlee, A.; Min, Y.; Tian, X.; Kim, Y. S.; Caster, J. M.; Zhang, L.; Zhang, T.; Huang, L.;
925 Wang, A. Z., *Biomaterials* **2016**, *82*, 178-93. DOI 10.1016/j.biomaterials.2015.12.018.

926 47. Lee, Y.; Park, S. Y.; Mok, H.; Park, T. G., *Bioconjugate chemistry* **2008**, *19* (2), 525-31. DOI
927 10.1021/bc700382z.

928 48. Yang, X.; Grailer, J. J.; Rowland, I. J.; Javadi, A.; Hurley, S. A.; Matson, V. Z.; Steeber, D. A.;
929 Gong, S., *ACS nano* **2010**, *4* (11), 6805-17. DOI 10.1021/nn101670k.

930 49. Xu, X.; Saw, P. E.; Tao, W.; Li, Y.; Ji, X.; Bhasin, S.; Liu, Y.; Ayyash, D.; Rasmussen, J.; Huo, M.; Shi,

931 J.; Farokhzad, O. C., *Advanced materials (Deerfield Beach, Fla.)* **2017**, *29* (33). DOI
932 10.1002/adma.201700141.

933 50. Muzza, M.; Pogliaghi, G.; Colombo, C.; Carbone, E.; Cirello, V.; Palazzo, S.; Frattini, F.; Gentilini,
934 D.; Gazzano, G.; Persani, L.; Fugazzola, L., *Cancers* **2022**, *14* (23). DOI 10.3390/cancers14235857.

935 51. Yang, X.; Yu, Y.; Wang, Z.; Wu, P.; Su, X.; Wu, Z.; Gan, J.; Zhang, D., *Frontiers in oncology*
936 **2022**, *12*, 968043. DOI 10.3389/fonc.2022.968043.

937 52. Zheng, H.; Xu, N.; Zhang, Z.; Wang, F.; Xiao, J.; Ji, X., *Frontiers in pharmacology* **2022**, *13*,
938 823975. DOI 10.3389/fphar.2022.823975.

939 53. Rosselgong, J.; Chemin, M.; Almada, C. C.; Hemery, G.; Guigner, J. M.; Chollet, G.; Labat, G.;
940 Da Silva Perez, D.; Ham-Pichavant, F.; Grau, E.; Grelier, S.; Lecommandoux, S.; Cramail, H.,
941 *Biomacromolecules* **2019**, *20* (1), 118-129. DOI 10.1021/acs.biomac.8b01210.

942 54. Tang, Y.; Li, Y.; Xu, R.; Li, S.; Hu, H.; Xiao, C.; Wu, H.; Zhu, L.; Ming, J.; Chu, Z.; Xu, H.; Yang, X.;
943 Li, Z., *Nanoscale* **2018**, *10* (36), 17265-17274. DOI 10.1039/c8nr04657c.

944